

RESEARCH ARTICLE

10.1002/2013JA019176

Key Point:

- Substorm current wedge is actually two-wedge systems

Correspondence to:

J. W. Gjerloev,
Jesper.Gjerloev@jhuapl.edu

Citation:

Gjerloev, J. W., and R. A. Hoffman (2014), The large-scale current system during auroral substorms, *J. Geophys. Res. Space Physics*, 119, 4591–4606, doi:10.1002/2013JA019176.

Received 28 JUN 2013

Accepted 11 MAY 2014

Accepted article online 15 MAY 2014

Published online 19 JUN 2014

The large-scale current system during auroral substorms

J. W. Gjerloev^{1,2} and R. A. Hoffman³

¹Applied Physics Laboratory—Johns Hopkins University, Laurel, Maryland, USA, ²Birkeland Centre, University of Bergen, Norway, ³Heliophysics Division, NASA/Goddard Space Flight Center, Greenbelt, Maryland, USA

Abstract We present an empirical model of the equivalent current system in the ionosphere during the peak of a classical bulge-type auroral substorm. This model is derived from measurements made by ~110 ground magnetometer stations during 116 substorms. The data are temporally and spatially organized using global auroral images obtained by the Polar Visible Imaging System Earth Camera. The empirical equivalent current system displays three key features: a poleward shift of the westward electrojet connecting the postmidnight and premidnight components; a polar cap swirl; and significantly different magnitudes of the postmidnight and premidnight westward electrojets. This leads us to propose a two-wedge current system linking the ionosphere to the magnetosphere. The bulge current wedge is located in the premidnight region just equatorward of the open-closed field line boundary while another three-dimensional current system is located in the postmidnight region well within the auroral oval. We use Biot and Savart calculations and Tsyganenko mapping and show that this new model is a likely solution for the large-scale current system.

1. Introduction

The magnetosphere and ionosphere are primarily coupled by electric currents and flows of charged particles along magnetic field lines. Currents in the ionosphere are the dominant phenomenon at ionospheric altitudes compared to all other phenomena pertaining to magnetosphere-ionosphere coupling, involving many times more energy dissipation than particle precipitation [Foster *et al.*, 1983; Lu *et al.*, 1998].

During the last 40 years numerous studies have investigated this three-dimensional current system of the auroral ionosphere and its coupling to the magnetosphere. Various fundamental current configurations and auroral electrojet components have been proposed, such as the substorm current wedge [McPherron *et al.*, 1973] and the two-component westward electrojet (WEJ) [Kamide *et al.*, 1982]. In the latter configuration the westward electrojet system was suggested to consist of the so-called directly driven and the unloading component [e.g., Kamide and Kokubun, 1996, and references therein]. Rostoker [1996] proposed a schematic model of the auroral electrojet configuration during substorms based on a phenomenological and theoretical framework. These models have commonalities as well as differences. For example, McPherron *et al.* [1973] associated the wedge with a disruption of the cross-tail current sheet, and since at that time no obvious reason existed why current disruption should occur at a preferred local time the current wedge was illustrated as symmetrical around midnight. The Kamide and Kokubun [1996] two-component electrojet concept still considered the substorm current wedge to be centered around midnight while, on the other hand, Rostoker [1996] produced a schematic illustration of the auroral electrojet system in which he predicted two WEJ components to be located premidnight and postmidnight and shifted in latitude. While these concepts have commonalities they also display fundamental differences that have profound implications regarding the magnetospheric origins of the currents.

Numerous studies of the ionospheric currents have been published based on the ground level magnetic field perturbations from the ionospheric currents during various conditions. Often these have been interpreted as being due to Hall currents, and a 90° clockwise rotation of the perturbation vectors has been used to derive a so-called equivalent current system. Early studies were typically based on local latitudinal profiles of the magnetic perturbations [e.g., Kisabeth and Rostoker, 1974; Wiens and Rostoker, 1975]. Subsequently the development of the KRM inversion technique [Kamide *et al.*, 1981] enabled more sophisticated methods and larger numbers of magnetometer stations to be used to derive a global ionospheric current distribution [e.g., Ahn *et al.*, 1995; Kamide *et al.*, 1982; Kamide and Baumjohann, 1985; Clauer and Kamide, 1985]. Later, additional ionospheric observations (e.g., auroral images derived conductivities) were included into the technique that became known as Assimilative Mapping of Ionospheric Electrodynamics (AMIE) [Richmond *et al.*,

1990]. The resulting current systems were, however, based on interpolations over large spatial data gaps, the inclusion of empirical statistical models (e.g., conductances [Kamide *et al.*, 1996]) and the use of various weights in defining the importance of the measurements obtained by very diverse platforms (e.g., satellites). While global, instantaneous patterns of electrodynamic parameters are appealing, one must remember that the solutions are based on the various assumptions and limitations of the technique and the models utilized. Attempts to synthesize data from the diverse types of observations and a large array of ground-based magnetometer observations to obtain instantaneous patterns of the ionospheric currents and electric fields using the AMIE technique probably reached its pinnacle with the studies by Kamide *et al.* [1996] and Lu [2000].

Addressing the spatial and temporal morphology of the auroral substorm and the underlying magnetospheric causes are complicated by the high spatial and temporal variability of the electrodynamic parameters. We can approach the problem using single events studies or large statistical studies. Single event studies cannot resolve the primary spatial structures of the current system since we currently do not have the required observational coverage. Statistical studies, on the other hand, are challenged by the differences between individual events (e.g., size and location) that lead to smearing out the features of interest. In attempting to overcome these obstacles, we have taken an entirely different approach using global auroral images to organize the ground-based magnetometer data. Effectively, we use the auroral emissions as a reference system instead of magnetic coordinates [see Gjerloev *et al.*, 2002]. This is not a new idea. In fact, the groundbreaking empirical substorm analysis performed by Akasofu [1964] was founded on the premise that, while each substorm is unique in details, all substorms have common large-scale features. Later, Frank *et al.* [1981] wrote in the description of the spin scan photometer flown on DE-1 “such imaging will provide a natural coordinate system...to reference in situ point measurements.” This technique is founded on the assumption that other fundamental ionospheric electrodynamic parameters (such as ionospheric currents, field-aligned currents, convection electric fields, and height integrated conductivities) also can be organized by the auroral emission patterns [e.g., Frank *et al.*, 1981; Fujii *et al.*, 1994; Gjerloev *et al.*, 2007]. Curiously, very few studies have attempted to relate the derived ionospheric current systems to the developing structures of the simultaneous auroral event. No quantitative technique was proposed that utilized these assumptions to combine data sets from multiple events until Gjerloev *et al.* [2008] developed a normalization technique that yields much improved spatial resolution without smearing the key features of the parameter of interest.

We utilize this technique in analyzing the ground magnetic field perturbations from 116 substorms to achieve two objectives:

1. Derive an empirical global ionospheric and field-aligned current system for the peak of a classical auroral substorm;
2. Determine if previously published substorm models are in agreement with the observational constraints determined in (1).

Section 2 of this paper describes the data utilized and explains the event selection criteria, which is the same event set used in Gjerloev *et al.* [2007]. Section 3 describes briefly the methodology of our analysis (normalization techniques). In section 4, we show our statistical average pattern and validate the results. Section 5 is an extensive analysis of our results, and section 6 is a discussion and a presentation of a new possible solution for the large-scale 3-D current system. A summary and conclusions are given in section 7.

2. Data

The primary data set used in this analysis is magnetic field perturbation vectors provided by the SuperMAG collaborators [Gjerloev, 2009, 2012]. For each event this typically includes ~110 ground-based stations located at magnetic latitudes from 40° to 90°. The data provided through the SuperMAG initiative have been cleaned, rotated into a local magnetic coordinate system, and the baseline has been subtracted. SuperMAG uses a local magnetic coordinate system where N is the local magnetic north, E is local magnetic east, and Z is down (for an extensive explanation, see Gjerloev, [2012]).

We further use global auroral images acquired by the Visible Imaging System (VIS) that was carried on the Polar satellite [Frank *et al.*, 1995]. The Earth Camera in this system provides global auroral images in far-ultraviolet wavelengths (passband is 124 to 149 nm). The temporal resolution was 1 to 5 min depending upon whether the Earth Camera was sharing the VIS telemetry allocation with the visible imager in the

same instrument. To ensure an onset timing of each event with a precision of ~ 1 min, the Earth Camera data were often supplemented with images from the visible imaging camera and the 1 min image data from the Ultraviolet Imager (UVI) on Polar [Torr *et al.*, 1995]. For our analysis, we preferred to use the VIS data over the UVI data due to its increased spatial coverage and accuracy. The combination of these data sets ensured correct onset identification and ensured that the substorm developed continuously out of the identified onset (elimination of pseudo onsets).

Events were selected using six criteria:

1. Temporally isolated event (optically and magnetically);
2. Spatially localized onset of the optical aurora;
3. Bulge-type auroral substorm;
4. Only events with a single expansion and recovery phase (in case of a secondary expansion the event end is defined as the time of the second expansion);
5. Entire auroral bulge region in darkness (solar zenith angles $> 104^\circ$ or 200 km altitude) to eliminate any terminator effects;
6. Not during magnetic storms ($|Dst| < 30$ nT) or periods of continuous long duration magnetic activity.

Criteria (1) ensures that the events were fairly isolated; (2) through (4) ensure that we only include one type of event—the classical bulge-type auroral substorm; (5) ensures the required spatial coverage needed to organize the ground magnetic field data (reference frame) and eliminates the need to address the role of the terminator. Finally, (6) excludes storm time events since it is currently unknown if the auroral electrodynamic is similar for storm and nonstorm time conditions [e.g., Hoffman *et al.*, 2010]. A total of 116 events from the years 1997 to 2001 were selected using the above criteria.

3. Methodology

In this section, we briefly explain how data are organized in space and time. We refer to the papers by Gjerloev *et al.* [2008] for an extensive explanation, validation and discussion of the method we use.

The three basic factors that complicate statistical studies of the auroral substorm are as follows:

1. The wide range in temporal evolution of auroral substorms from a few tens of minutes to several hours [Gjerloev *et al.*, 2007; Pellinen *et al.*, 1994];
2. The variation in local time position of auroral features from event to event, for example, the magnetic local time (MLT) variation in the location of the head of the surge at the peak of the substorm [Gjerloev *et al.*, 2007, and references therein];
3. The high variability in the extent of the poleward expansion [e.g., Gjerloev *et al.*, 2007a].

These complexities effectively eliminate the possibility of using a standard coordinate system (e.g., the magnetic local time and magnetic latitude) to organize our events as this would unavoidably lead to smearing of the features being investigated.

To minimize the effects of these variations between substorms, we have developed a normalization process that is essentially a pixel mapping from the original auroral images to a normalized coordinate system [Gjerloev *et al.*, 2007]. The normalized coordinate system is derived from the average auroral emission pattern. The technique allows the transformation of any parameter from the magnetic coordinate system to the normalized coordinate system. All that is needed is a geomagnetic location of a particular pixel, such as a magnetic perturbation vector and an image of the global auroral emissions. In this way the magnetic perturbation vectors for each of the 116 events were utilized to derive a statistic pattern including a total of ~ 4500 measurements.

This mapping uses a three-step normalization process (one temporal and two spatial).

- Step 1: Normalize the timescale of the substorm ($T=0$ is onset and $T=1$ is maximum expansion);
- Step 2: Normalize the local time extent and position of the auroral bulge;
- Step 3: Normalize the latitudinal extent and position of the auroral oval.

Again, we refer to the Gjerloev *et al.* [2007] paper for an extensive discussion and validation of this powerful technique. For here the main point to recall is that while it is cumbersome compared to simply using magnetic coordinates, it very effectively minimizes smearing.

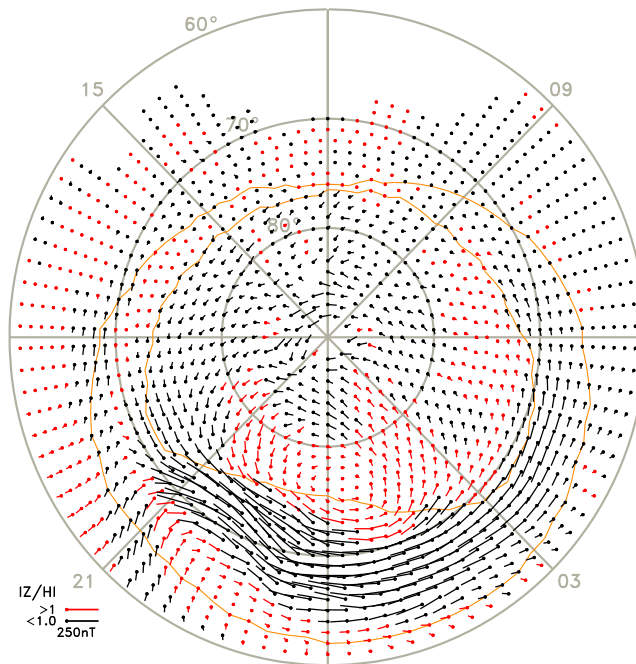


Figure 1. Polar plot showing equivalent currents at the peak of a bulge-type substorm. Coordinates are magnetic latitude and magnetic local time. Units are nT and the measured perturbations are rotated 90° clockwise to indicate the equivalent current direction. Colors indicate the ratio of the horizontal and vertical components ($H = (N^2 + E^2)^{1/2}$).

The temporal normalization (Step 1) eliminates smearing due to the differences in expansion phase duration. The first brightening or expansion phase onset is defined as $T = 0$ and the peak of the substorm is $T = 1$. Our selection of these times is thus based purely on the global auroral images. The substorm peak is based on a qualitative estimate of the combined intensity of the event and the westward and poleward expansion of the poleward auroral boundary. Although this differs from the usual identification using the AL index, Gjerloev *et al.* [2007] found that the AL on average minimizes at $T \sim 1$ indicating that on average the westward auroral electrojet does indeed peak at the same time as the optical substorm.

Normalization of the local time (Step 2) eliminates smearing due to varying local time position and size of the auroral bulge. We position it in local time by squeezing/stretching each bulge to match the average size. These average values were determined by Gjerloev *et al.* [2008, Table 1].

Finally, the latitudinal normalization (Step 3) eliminates smearing due to the varying latitudinal location and width of the auroral oval. This is done in a way similar to the above MLT normalization although it requires a nontrivial determination of the low- and high-latitude auroral boundary [Gjerloev *et al.*, 2008].

Although these normalizations may appear complex, they are essentially coordinate system transformations—from a magnetic local time and latitude coordinate system to an auroral emissions reference system. This normalization method or advanced superimposed epoch analysis can be performed with any type of data with known positions acquired at the same time as the images.

4. Statistical Results

In this section, we present the results for the equivalent current pattern as well as two validation plots.

4.1. Normalized Current Pattern

Figure 1 contains the average equivalent current pattern at the peak of the substorm. This pattern is deduced from the 116 events including a total of 4536 ground-based magnetometer measurements. Empirical auroral oval boundaries are superposed onto the magnetic field perturbations as red lines (see Gjerloev *et al.* [2008] for an explanation of how these boundaries were determined).

For the reader to understand the plot, we wish to point out a number of important issues:

1. We rotate the horizontal magnetic field perturbations 90° clockwise to indicate the equivalent ionospheric current direction.
2. The spatial resolution of these polar plots is variable:
 - a. Below 60° latitude: 3° latitude by 4° longitude.
 - b. 60°–70° latitude: 1° latitude by 4° longitude.
 - c. Above 70° latitude: 1° latitude but with a variable number of longitudinal bins for a constant area binning

3. Weighted smoothing has been applied to the data. Each pixel is averaged with the four surrounding nearest neighbor pixels using a weighting of 1 for the center pixel and 0.5 for each of the surrounding pixels.
4. The vectors are plotted in three colors, depending upon the absolute value of the ratio of Z to H. A color change from black to green or black to red indicates the boundary of the horizontal current [see *Kisabeth and Rostoker, 1977*].
5. An individual event can only contribute a single measurement to a normalized pixel. If two or more closely spaced ground magnetometer stations contributed to a pixel, we first averaged these before using the data. This ensures that a single event cannot bias the result.
6. To simplify the interpretation of our results, we only include data from a ground magnetometer if it is in darkness (zenith angle is $> 104^\circ$). It may not be clear why this simplifies the interpretation, but for now we simply point out that this eliminates any effects associated with the terminator. Effectively our empirical models are applicable to winter conditions. The implications are further discussed in the discussion section below. Examples of the magnetometer data superposed on auroral images are shown in Figure 2.

Finally, we do not convert the measurements from units of nT to a current density since this conversion would require assumptions on the ionospheric conductance. However, if desired the reader can convert our statistical results from nT to Ampere using the relationship where a measured ground perturbation of 1 nT km is roughly equivalent to 2 A [from *Kamide et al., 1982*]. Further, it should be noted that our equivalent current pattern shown in Figure 1 might not be strictly divergence free. This is a strict requirement under the assumption of no instrumental noise and no statistical uncertainty.

4.2. Validation of Empirical Model

While the general technique has been carefully validated in previous papers [e.g., *Fujii et al., 1994*; *Gjerloev et al., 2008*], this section addresses the fundamental question: To what extent does our statistical pattern represent a typical event? Statistical average models are derived from a list of individual events but may not represent any of the events. An average may represent a mode of the system that never exists. The purpose of our empirical model is to reproduce the large-scale ionospheric current system and its coupling to the magnetosphere. It has been shown [e.g., *Fujii et al., 1994*; *Gjerloev and Hoffman, 2000*] that the auroral electromagnetic parameters are spatially organized by the auroral emissions. The intensity (e.g., as measured by AL) may differ between events, but the spatially normalized distributions of a given electromagnetic parameter are similar. Thus, we here investigate how well the average equivalent current pattern shown in Figure 1 represent the individual events. To answer this basic question, we determine the variability of the direction of the magnetic perturbation vectors within each bin. As a measure of this variability, we calculate the parameter:

$$\psi = \frac{1}{N} \sum_{i=1}^N \frac{\bar{T}_i \cdot \bar{T}_{ave}}{|\bar{T}_i| \cdot |\bar{T}_{ave}|}$$

where N is the number of vectors within the bin, \bar{T}_i is the measured vector within the bin, and \bar{T}_{ave} is the average vector. As seen, $\psi \in [-1, +1]$ where -1 indicates antiparallel and $+1$ indicates parallel. Although this quantity does not account for the variations in the magnitude of the vector, we argue that while the intensity of currents varies from event to event, the basic pattern is maintained. Hence, the quality of the average vector is defined by the vector direction not the magnitude.

Figure 3 shows the ψ parameter using a color scale with values ranging from 0 to 1. We can recognize a region of high correlation (0 to 6 MLT and 62 to 70 MLAT (magnetic latitude)) as associated with the postmidnight WEJ. At subauroral latitudes located ~ 21 MLT, we find another region of very high correlations indicating that basically all events display the same ground magnetic field perturbations. The quality of the normalization process is, however, best revealed by the dark, narrow region (poor correlation) between 60° and 70° in the premidnight sector. A comparison with the current vectors in Figure 1 shows that it is coincident with the Harang region or separation of the overlapping eastward and westward electrojets. Given that we include 116 events with large variations in the bulge position and size, we argue that this remarkably narrow region of uncertainty provides a powerful argument for the success of our normalization technique and validates our results. We also note the small "spot" of poor correlations around midnight and 77 MLAT, which is the center of the polar cap swirl (see section 5.3) where the magnitude of the magnetic perturbations become very small.

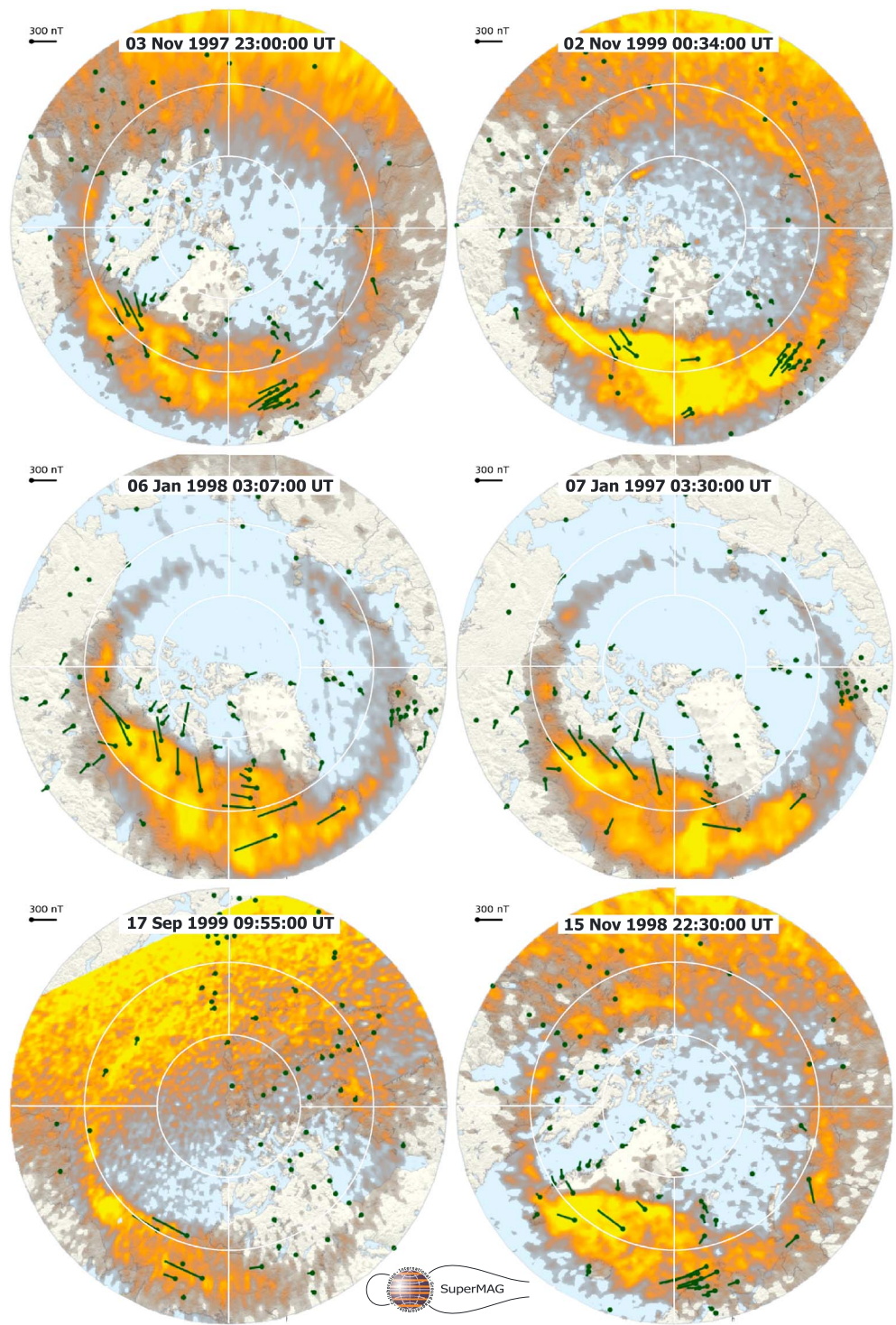


Figure 2. Four Polar VIS Earth camera images with ground magnetic field perturbations superposed (rotated 90° clockwise). These typical events are discussed in the paper. Plots are downloaded from the SuperMAG website.

Finally, we show the number of records in each bin for $T=1.0$ in Figure 4. The coverage is rather good in the auroral oval. The drop in coverage below 80° on the dayside is due to the darkness requirement (see section 6.2 for a discussion of the implications of this requirement).

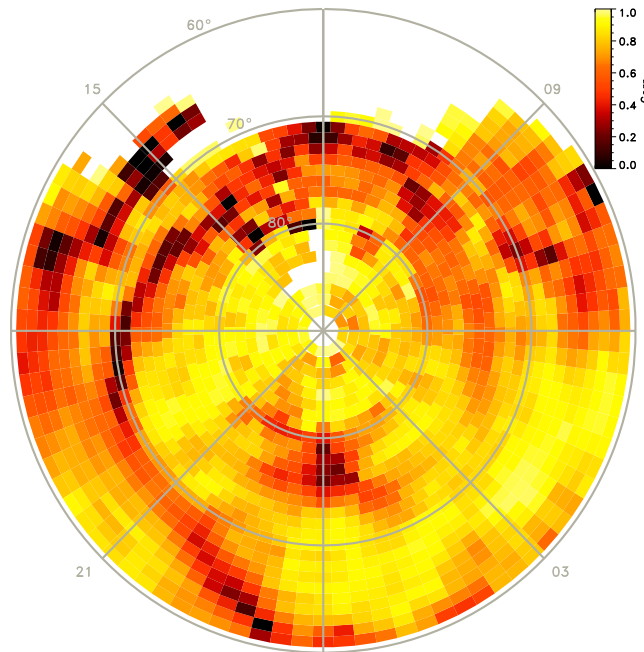


Figure 3. The ψ parameter (see text for details) showing the variability of the measurements within each pixel.

current wedge (BCW) and the oval current wedge (OCW). In section 6.2, we provide a rationale for these names. The purpose of these simulations is to determine whether either of these two fundamentally different current configurations can replicate large-scale key features seen in our model results (Figure 1). Thus, we ask the basic question: Can a single-wedge system reproduce the key features seen in our empirical model or are two wedges required? We could simulate the most simple current wedge system consisting of a single

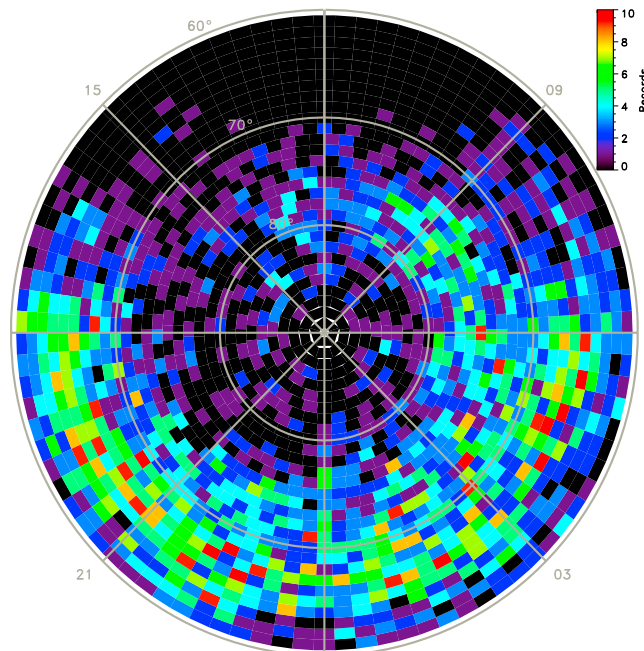


Figure 4. Number of measurements in each pixel.

5. Analysis

For the following discussion, we first show a schematic of two current configurations (Figure 5). The purpose of the figure is to illustrate two simple wedge solutions coupling the westward electrojet system to the magnetosphere. For clarity of the concept the drainage and feeding of the electrojets are shown as simple line currents.

5.1. Biot and Savart Calculations of Two Basic Current Configurations

To assist in the interpretation of our results, we first perform Biot and Savart simulations of two possible large-scale current configurations, a single-wedge system, and a double-wedge system. The former can be regarded as the classical substorm current wedge while the latter consists of 2 three-dimensional current wedges which we refer to as the bulge

wedge (BCW) and the oval current wedge (OCW). Obviously this system cannot reproduce the pronounced poleward displacement seen in the ground magnetometer data. On the other hand, we could determine a complex current distribution that produces a ground magnetic field distribution essentially identical to our empirical model. We chose a middle ground, relatively simple models that produce the key features.

Each 3-D current wedge system consists of ionospheric Hall currents flowing at an altitude of 105 km and connected to the magnetosphere by currents that flow along field lines as described by a Tsyganenko 89 model ($Kp = 2$). We have used a relatively low Kp since our results are for the peak of a substorm and thus the field

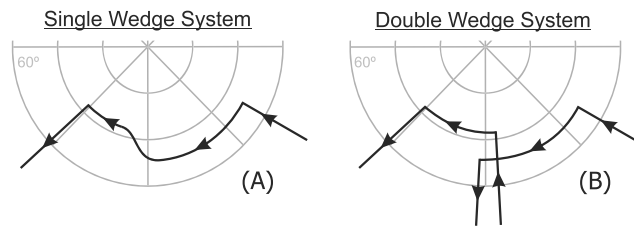


Figure 5. Two schematic large-scale current configurations: (a) The classical single current wedge system; and (b) Two current wedge systems shifted in local time and latitude. Note that only the net field-aligned currents and the ionospheric Hall currents are shown.

configuration should have undergone dipolarization. Neither our simulations nor our empirical model includes the Pedersen currents or the field-aligned currents (FACs) linking these Pedersen currents to the magnetosphere.

The one-wedge system we will consider consists of a series of ionospheric line currents (Hall) each separated by 1° MLAT (Figure 6a, left). Each line current is fed by a field-aligned line current at its east end and drained by a field-aligned line current at its west end (of equal strength). Both FACs are mapped to the magnetosphere equatorial plane using the Tsyganenko model. The WEJ makes a characteristic poleward displacement around midnight to connect the latitudinally shifted pre-midnight and post-midnight line currents. This system is conceptually the same as the classical three-dimensional substorm current wedge with feeding post-midnight and drainage pre-midnight. Our model, however, differs from the simple classical substorm current wedge in two aspects: Distributed feeding/drainage and the poleward displacement in the westward electrojet and, therefore, different magnetic latitudes of the feeding and drainage field-aligned currents. We are not aware of anyone having proposed such a single-wedge current distribution before, but these changes from the classical substorm current wedge are required to qualitatively reproduce the observed ground level perturbations.

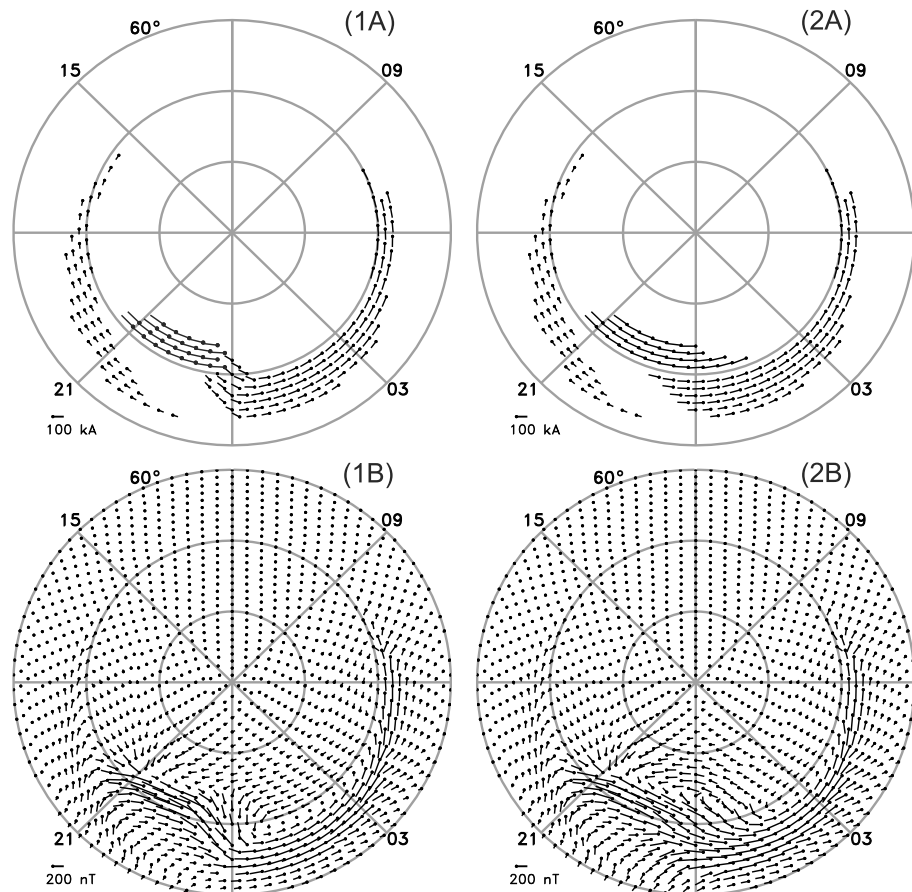


Figure 6. (top) Current configuration and (bottom) resulting ground level perturbations for the one-wedge system (left) and the two-wedge system (right).

The two-wedge system is identical to the one-wedge system except in the midnight region (Figure 6b). The postmidnight and premidnight WEJ components flow at constant latitude and are completely separated as there are no currents flowing at 70° MLAT. We refer to the higher latitude set as the bulge current wedge, BCW, and the lower latitude set as the oval current wedge, OCW. In the midnight region the drainage of the OCW occurs at a lower latitude than the feeding of the BCW. The total current at 22 MLT and at 2 MLT (before and after the midnight displacement) is identical in both the single-wedge and the two-wedge simulations. This is in conflict with our findings that the OCW carries roughly twice the current of the BCW (see section 5.2.2). However, it was done to simplify the comparison between the two wedge solutions.

The eastward electrojet configuration is identical in the two simulations.

As a final note on the use of these simplistic simulations, we do wish to emphasize that the purpose is not to provide “evidence” of one or the other solution. We realize their limitations, and as we stated in the beginning of this section, they are simply meant to “assist” us in the interpretation of our results shown in Figure 1.

5.2. Comparison of Key Characteristics

5.2.1. Latitudinal Displacement of the Westward Electrojet

A striking feature seen in Figure 1 is the poleward shift of the WEJ in the premidnight region from a rather constant latitudinal profile commencing around dawn. The shift is ~5–6° in latitude from a location well within the auroral oval (postmidnight) to a location just inside the poleward edge of the oval (premidnight). To illustrate that this is not a statistical artifact, we refer back to the six typical events shown in Figure 2. The events with appropriate station locations clearly show a postmidnight WEJ maximizing at much lower latitudes than the premidnight component.

From the two Biot and Savart simulations shown at the bottom of Figure 6, we see that both wedge solutions produce a poleward displacement in the equivalent current distributions (actually ground magnetic field perturbations rotated 90° clockwise). It is expected that the one-wedge system would produce the poleward displacement, since the ionospheric current has a comparable shift. It is, however, surprising that the two-wedge system also produces the poleward displacement since the BCW and the OCW components flow along constant latitudes. The angle is a result of ground perturbations produced by the FACs and underlines the importance of taking care in interpreting the ground level perturbations as solely overhead currents.

We can find support for this poleward shift in previously published models. The Boundary Layer Dynamics model by *Rostoker* [1996] is of interest since to a large extent it is deduced on the basis of ground magnetometer observations. His two WEJ components are completely separated in latitude and are roughly located at 22:00–08:00 MLT and 15:00–23:00 MLT. The latitudinal shift is in good agreement with our observations.

Allen and Kroehl [1975] found the typical position of the AL contributing station during substorms to be 03:00 MLT. It is interesting to note that only three of the 11 stations they utilized did contribute to the AL when located premidnight. These three stations were all located above 69.3° CGM (corrected geomagnetic) latitude while the remaining stations, which never contributed premidnight, were located below 68.4°. We can explain their results as due to a latitudinally shifted WEJ system as found in this paper.

Finally, the studies by *Kamide et al.* [1996] and *Kamide and Kokubun* [1996] showed the ionospheric current configuration during different stages of a substorm. In good agreement with our results they found the peak in the postmidnight WEJ to be located at 66° MLAT while the premidnight maximum was found to be located at 71° MLAT.

5.2.2. Polar Cap Swirl

Within the polar cap, Figure 1 shows a distinct vortex with a center at 74° MLAT and midnight, bounded by the poleward edge of the westward electrojet and extending past 80° MLAT (red vectors with a considerable patch of green past 3 MLT). This curious and consistent new feature encompasses most of the polar region, with much of the swirl completing its rotation into the east end of the BCW. This feature can also be found in the individual examples (see Figure 2) and is thus not a statistical artifact.

From the two Biot and Savart simulations, we see that both wedge solutions produce poleward pointing vectors at the head of the surge as expected, since at this MLT the current wedges are the same. However, only the double-wedge system produces equatorward pointing vectors around 1 MLT in the polar cap. This feature is due to the downward FACs present above 70° MLAT that feed the higher latitude BCW in the two-wedge solution, which are missing in the single-wedge system.

Our simulations further show that perturbations in the polar cap can be attributed to FACs flowing at auroral latitudes giving red-colored vectors. Thus, ground level magnetic field perturbations are not necessarily due to overhead ionospheric currents. The reason is simple. There is neither the necessary conductivity nor any large-scale convection pattern that would drive a current producing the swirl. The red boundaries shown in Figure 1 are the average oval boundaries as identified from Polar VIS images for all 116 events. Poleward of the bulge the images show virtually no emissions indicative of very soft particle precipitation leading to very low conductances [also see *Wallis and Budzinski, 1981; Gjerloev and Hoffman, 2000*]. Thus, we argue that perturbations measured by the stations located within the polar cap are largely due to the FACs flowing into the auroral zone. As we did in section 5.1, we again argue that care must be taken in interpreting ground magnetic observations as being indicative of overhead ionospheric currents alone.

Thus, we show that the poleward displacement is not necessarily associated with a similar poleward displacement in the electrojet current but can be produced by two separate wedge systems. While our single-wedge solution, which includes a poleward displacement of the WEJ, has never been proposed before, there has not been empirical evidence that would suggest such a configuration until now. We argue that the displacement in the ground perturbations requires a new solution, and thus, these two simple simulations are more than simple numerical exercises.

5.3. Westward Electrojet Current Continuity

In the single-wedge solution the total electrojet current at a latitudinal cross section before and after the displacement must match (assuming no feeding or drainage within the displacement). In the two-wedge solution this is not required since there is no reason to believe that the total electrojet current in the OCW should be the same in the BCW. In our model (Figure 1), we estimate the total current by a simple summation of the black vectors ($|Z/H| < 0.5$) for a latitudinal cut and find the total to be ~1200 nT at 2 MLT and ~750 nT at 21 MLT. The discrepancy is striking. This implies that at least 40% of the postmidnight WEJ must be drained in the midnight region but it could also be 100%.

Gjerloev and Hoffman [2002] used Dynamics Explorer satellite observations to derive an empirical model of the auroral current system. They found that the total current at 2 MLT was 315 kA and only 145 kA at 21 MLT [*Gjerloev and Hoffman, 2002, Figure 5*]. They further found that only 60 kA was provided by the postmidnight WEJ to the premidnight WEJ. Thus, ~60% of the total current drained at 21 MLT must be provided by downward FACs in the high-latitude premidnight region. Approximately 80% of the postmidnight WEJ must be drained near midnight by upward FACs. These findings all appear to be in conflict with the single-wedge solution and support the two-wedge solution.

In the Biot and Savart simulations, we assumed total WEJ current continuity and that the postmidnight and premidnight currents are the same. The reason for this assumption was that in order to compare the two solutions we must minimize the differences between them.

5.4. Tsyganenko Mapping

To further explore the implications of the two solutions, we trace field lines from the drainage and feeding regions in the ionosphere to the equatorial plane of the magnetosphere. We use a Tsyganenko 89 model with $Kp = 2$ and $Kp = 4$. It is well known that magnetic field line mapping during substorm conditions is associated with considerable uncertainties [e.g., see *Donovan, 1993*]. We therefore emphasize that the purpose of this mapping is to get rough qualitative information regarding the spatial distribution of the magnetospheric source region. It should be kept in mind that the uncertainties in the mapping decrease toward lower L shell.

For the single-wedge system, we use two points: 3.5 MLT/65° MLAT and 21.5 MLT/71° MLAT. The points are determined from Figure 1, and we map these positions to the equatorial plane in the magnetosphere.

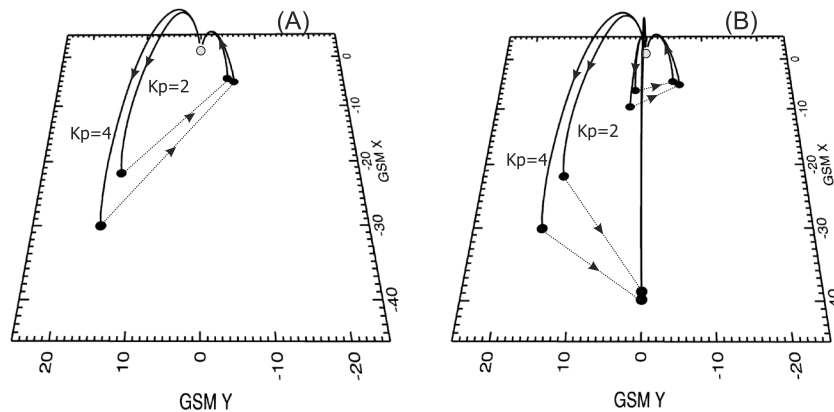


Figure 7. Mapping of WEJ feeding and drainage regions from the ionosphere to the equatorial plane of the magnetosphere. A Tsyganenko 89 model is used with two different K_p levels (2 and 4).

Figure 7 indicates a magnetospheric closure current strongly skewed along the X axis. In other words, the mapping indicates that a single-wedge system is not due to a diversion of the cross-tail current.

For the two-wedge system, we use the same end points but add drainage FACs at 23.0 MLT/65° MLAT and feeding FACs at 24 MLT/71° MLAT. The mapping of the BCW now appears to be in reasonable agreement with a diversion of the cross-tail current. For the OCW the closure is located deep in the inner magnetosphere. Thus, the two magnetospheric closures are far apart.

For the single-wedge system, one may argue that it could not be expected that the current show no X dependence across a large Y range. It may be further argued that the Tsyganenko modeling should not be used for substorm conditions as the field configuration undergoes large changes in a matter of minutes. We agree with both points. We, however, point out that the location of the currents relative to the auroral emissions provides important information regarding the mapping and some support to the above findings. The OCW flows well within the oval and the BCW flows just equatorward of the open-closed field line boundary, so we argue that these currents must map to vastly different regions of the magnetosphere.

The two-wedge model has some important and testable implications for the distribution of the magnetospheric sources. The center of the two wedges is shifted in the Y -GSM direction as well as in the X -GSM direction. The BCW is predominantly located premidnight while the OCW covers the midnight to postmidnight region. This has implication for the magnetospheric sources of these current systems, and our model indicates that the processes or signatures related to the auroral bulge expansion (the bulge current wedge) must be statistically shifted toward the + Y -GSM direction. This is in excellent agreement with the study by *Sigsbee et al.* [2005] who identified 65 dipolarizations using the Wind spacecraft. They concluded that most of the events occurred in the premidnight region of the magnetotail. This asymmetry was more pronounced for the isolated events than for the events that occurred as part of a series. This is in agreement with *Miyashita et al.* [2003] who concluded from a statistical magnetotail study that the merging of magnetic field lines predominantly occurs premidnight.

Wing et al. [2007] derived 2-D distributions of the plasma sheet pressure as a function of substorm phase. They used DMSP particle precipitation measurements that were mapped to the equatorial plane. Interestingly they also found a distinctly asymmetric distribution where the pressure peaks in the postmidnight region of the inner magnetosphere during the early to late recovery phase. During the expansion phase, there are indications that the pressure peaks in the premidnight region.

5.5. Basic Current Configuration

Figure 8 shows a conceptual illustration of the two-wedge system. Figure 8a is a close-up and Figure 8b shows the mapping to the magnetosphere. Only the basic components are shown—the net FACs and the ionospheric Hall currents. Thus, we do not include the energy dissipating Pedersen currents or the FACs coupling these to the magnetosphere. Notice that the feeding and drainage is shown to be distributed in MLT. These FACs are shown as simple sheet currents. The figure assumes complete separation between the two wedge systems.

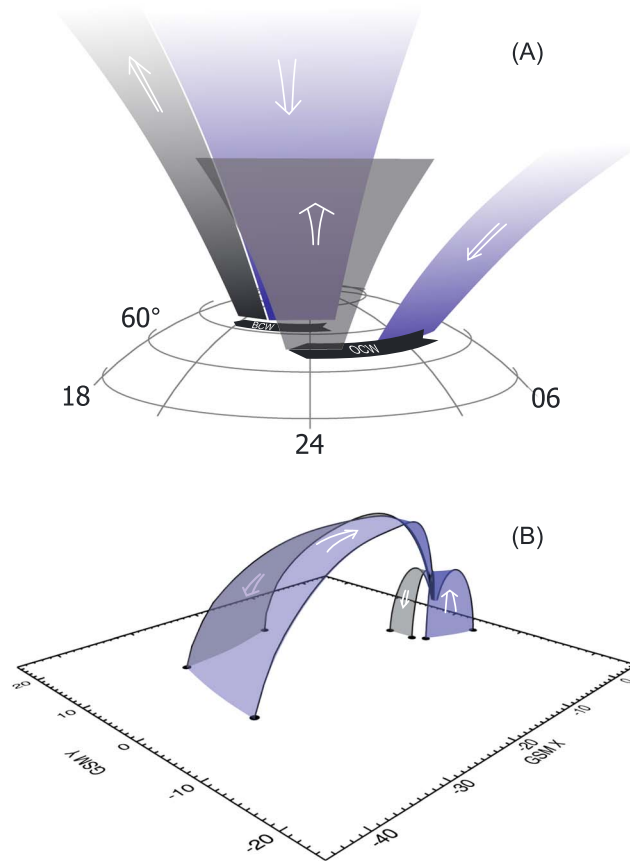


Figure 8. Schematic illustrations of the proposed two-wedge model. Only net FAC's and ionospheric Hall currents are shown. (a) Note that the feeding and drainage is distributed in MLT. (b) Mapping to the magnetospheric source region using a Tsyganenko 89 model with $K_p = 2$. FACs flowing out of the ionosphere are grey while FACs flowing into the ionosphere are blue.

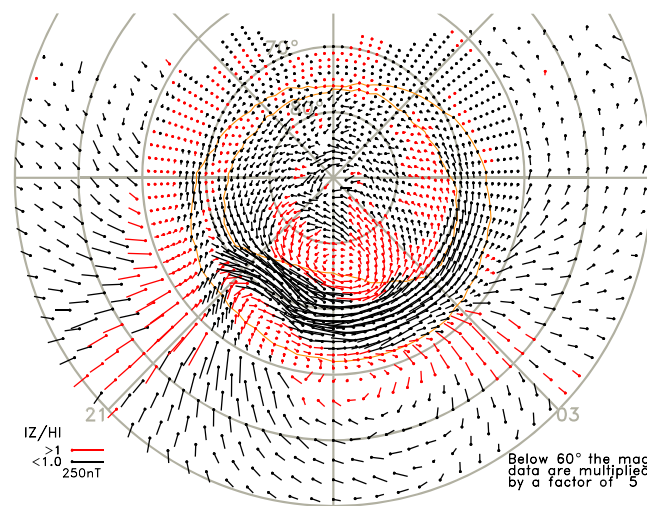


Figure 9. Polar plot showing equivalent currents at the peak of a bulge-type substorm (same format as Figure 1). Note that below 60° magnetic latitude the vectors are multiplied by a factor of 5.

5.6. Subauroral Perturbations

Figure 9 shows the subauroral perturbations, while Figure 10 contains the distribution of the Ψ parameter. Historically, the subauroral perturbations have been interpreted as an indication of the feeding and drainage of the auroral electrojets. [e.g., Clauer and McPherron, 1974]. In the following discussion, we focus on the subauroral region. Here southward or northward vectors indicate outward or inward drainage via field-aligned currents, respectively.

Figure 9 indicates a clear intense drainage of the westward electrojet with a sharp westward cutoff of the drainage region at 21 MLT, where the vectors change from black to red at all latitudes from 40° to 60°. Similarly, there appears to be a broader region of input current extending from around 02.5 MLT to dawn. In between the red vectors indicate some signs of uncertainty in direction.

Figure 10 shows that virtually all vectors in the 21 MLT region indicate drainage (yellow or $\Psi \sim 1$). From 2.5 MLT to dusk in the subauroral region, the Ψ parameter has values slightly lower, but show that most vectors indicate feeding. In between, the values are much lower, indicating that the direction of the vectors vary from event to event.

At first glance the interpretation of Figure 9 is that the feeding in the postmidnight region is connected to the drainage in the premidnight region through the westward electrojet current. This would be the case for the classical single-wedge system. However, we argued above that this is inconsistent with a poleward displacement in the westward electrojet. A single-wedge system will result in $\Psi \sim 1$ around 21 MLT and 3 MLT but it cannot reproduce $\Psi \sim 0$ in the midnight region.

In our double-wedge system, the drainage and feeding of these two current wedges can overlap (see

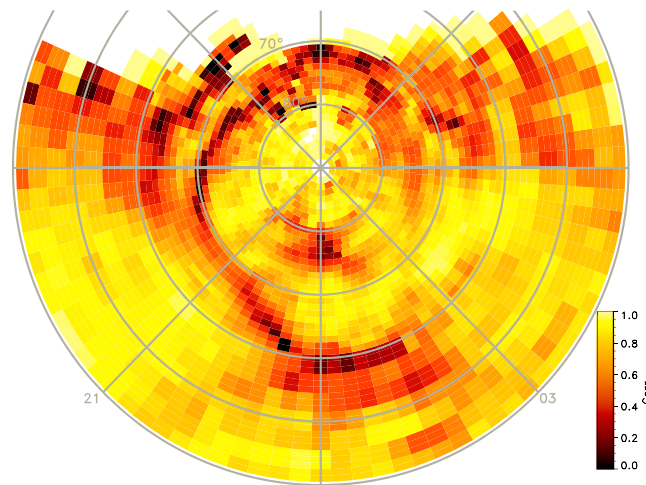


Figure 10. The ψ parameter (see text for details) showing the variability of the measurements within each pixel.

Figure 5 for a simple schematic illustration), thereby complicating the interpretation of data from ground stations around midnight. The intensity and relative location of these feeding/drainage currents vary from event to event resulting in low ψ values.

6. Discussion

6.1. Why Are the Postmidnight and Premidnight WEJ Components Disconnected?

At ionospheric altitudes, the key difference between the two wedge configurations lies in the midnight region WEJ. Here we must discuss the possible reasons for a decoupling between the postmidnight and

premidnight WEJ components. We consider the conductance and convection electric field distributions since the WEJ is a function of these parameters [Kamide and Kokubun, 1996]. The key region is the midnight region where these two distributions either support WEJ current continuity or provide an argument for a decoupling. However, the hypothetical decoupling of the two WEJs must be supported by the conductance and the convection electric field distributions. A derivation of these distributions is not possible using only ground-based magnetometers.

6.1.1. Conductance Distribution

In the examples shown in Figure 2, we note indications of bright auroral emissions in the postmidnight region at around 65° and another region of bright emissions in the premidnight region but at higher latitudes. The two regions overlap in local time but are separated in latitude by a valley of less intense emissions. If we make the simplistic assumption that the emissions are indicative of the Hall conductance, this finding indicates a valley of low conductance. Gjerloev *et al.* [2007] performed a statistical study of the emissions from all of our 116 substorms. It was noted that a valley did indeed exist. They went further and fitted the latitudinal cross section by a function consisting of two Gaussians. In the midnight region two distinct peaks were found to exist at the same MLT.

The ionospheric conductance can be derived from two separate wavelengths of the auroral emissions if we use a number of simplifying assumptions. Above we made the gross assumption that the emissions are indicative of the conductance distributions and made some qualitative arguments. Another technique calculates the conductivity profile from measurements of precipitating electrons [Rees, 1963]. Gjerloev and Hoffman [2000] used electron precipitation measurements made by the Dynamics Explorer 2 (DE2) satellite to derive the global conductance distribution. They found two regions of high Hall conductance very similar to the above findings. The Hall conductance in the valley was a factor ~ 2 lower (~ 12 mho) than the two high Hall regions (~ 25 mho). Qualitatively, similar results can be found in the studies by Spiro *et al.* [1982] using AE for binning and Wallis and Budzinski [1981] using K_p .

6.1.2. Convection Electric Field Distribution

The other parameter that plays a role in the possible coupling or decoupling of the two WEJ components is the convection electric field. Gjerloev and Hoffman [2001] derived the global convection electric field distribution using measurements made by the Dynamics Explorer 2 (DE2) satellite (same database as that used in the conductance study by Gjerloev and Hoffman [2002]). They found a distinct region of very low fields in the premidnight region. They referred to this as the "Harang region" rather than the conventional Harang discontinuity, which separates poleward fields at lower latitudes and equatorward fields at higher latitudes. This Harang region effectively serves as a termination of any postmidnight WEJ. Unfortunately, malfunctions in DE 2 instrumentation made it impossible to determine if a poleward WEJ component existed in the midnight region.

Grocott *et al.* [2002] performed an event analysis using SuperDARN, ground-based magnetometers and Polar VIS Earth Camera images to study the convection pattern during the evolution of a small substorm.

Despite relatively steady IMF conditions, they found significant changes to the convection pattern following the onset. This was supported by the statistical study by *Provan et al.* [2004] also using SuperDARN. They found a distinct region of suppressed convection within the bulge in excellent agreement with the Harang region [*Gjerloev and Hoffman, 2002*]. In their global patterns there is no reason to believe that the convection pattern provides a means for closing the postmidnight WEJ to the premidnight WEJ. In fact, the low convection region in the bulge would provide a termination of the postmidnight WEJ.

6.2. Implications Regarding Substorm Terminology

In the review paper by *Kamide and Kokubun* [1996], it was argued that the westward electrojet system during substorms consists of two components: the “convection electrojet” and the “substorm expansion electrojet”.

The “convection electrojet” is supposedly controlled primarily by solar wind magnetosphere interactions (e.g., merging and viscous effects). It is referred to as the directly driven component thereby indicating that it is primarily controlled by the solar wind driver. Logically it must be introduced at the southward turning of the propagated interplanetary magnetic field (IMF) B_z and be present as long as the IMF stays southward. But a so-called “directly driven” system must turn off when the driver disappears. *Kamide and Kokubun* [1996] address this critical question by suggesting that this may be due to neutral wind-ionosphere coupling (the so-called flywheel effect, e.g., *Lyons et al.* [1985] and *Aruliah et al.* [1999]). This places the generator in the thermosphere-ionosphere and implies that the hour-long decay of the current is supported by energy from this altitude.

Also, according to *Kamide and Kokubun* [1996] the “substorm expansion electrojet” is referred to as the unloading component and is due to substorm processes. These are internal to the magnetosphere and are centered in the midnight sector. They point out that the substorm expansion electrojet has a shorter lifetime than the convection electrojet but is more intense. The latter is supposedly “electric field dominant” while the former is “conductivity dominant”. This implies a cause and effect. Processes internal to the magnetosphere accelerate precipitating electrons leading to enhanced ionospheric conductance (unloading component) while the convection electric field supposedly is controlled by the solar wind driver (convection component). This is thus in agreement with the above terminology.

These arguments for underlying causes raise some difficult questions: (1) To what extent can we determine the causality (internal versus external) from the conductance and the convection electric field patterns? (2) Is the particle precipitation in the convection electrojet also controlled by the solar wind? If this is not the case then the ionospheric conductance is not directly controlled by the solar wind driver and thus neither is the WEJ. (3) Is the convection electric field driving the unloading electrojet due to internal processes?

To avoid these complexities we have chosen another approach. The two observational facts to which we can relate are the particle precipitation characteristics and their relative latitudinal position. Thus, we suggest to use these for a naming convention. The OCW is located within the diffuse aurora where the precipitation originates in the inner magnetosphere central plasma sheet, the CPS [*Winningham and Heikkila, 1974*]. The BCW is located just equatorward of the open/closed field line boundary and is associated with inverted V type precipitation that maps to the boundary plasma sheet, BPS, earthward of the near Earth neutral line. Both the BCW and the OCW are associated with energy released from the magnetosphere and deposited in the ionosphere. The BCW-associated energy is released as the magnetic field configuration changes while the source for the OCW is the plasma sheet plasma. Thus, the BCW is caused by processes in the BPS and the OCW by processes in the CPS region. Following the suggestions of *Rostoker* [1996], the BCW is associated with substorm processes such as reconnection and that the OCW is associated with plasma sheet pressure distributions. However, since both occur within the envelope of what we call a substorm, there must be some coupling between the two. The different regions of the WEJ system (we refer to the OCW and the BCW) are associated with different regions in the magnetosphere and different energy storage and release processes, and we speculate that this further argues for a dual wedge system. It seems illogical that a single-wedge system can be associated with different magnetospheric regions and different underlying processes.

If the BCW and the OCW are due to different magnetospheric causes, we can speculate that their relative intensity and temporal behavior are likely to differ from event to event. An event in which the OCW is insignificant would still be referred to as a classical bulge-type substorm, but an event where the BCW is

insignificant would be another type of event. The relationship between the onset (location and timing) and the two current systems is a topic that will be explored in subsequent papers.

7. Summary and Conclusions

We presented an empirically derived model of the equivalent current system during the peak of a classical bulge-type substorm. This model was derived from measurements made by ~110 magnetic observatories during 116 substorms. The data were temporally and spatially organized using global auroral images obtained by Polar VIS Earth Camera. The empirical equivalent current system derived from this organization of the data display three key features: a poleward shift of the westward electrojet connecting the postmidnight and premidnight components; a polar cap swirl; and postmidnight and premidnight westward electrojets that appear to have significantly different magnitudes. This led us to propose a two-wedge current system for the westward electrojet linking the ionosphere to the magnetosphere: a bulge current wedge located primarily in the premidnight region just equatorward of the open-closed field line boundary and another three-dimensional current wedge system located in the postmidnight region well within the auroral oval. We refer to this latter wedge as the oval current wedge. We used Biot and Savart calculations with Tsyganenko mapping to show that this new model is a likely solution for the large-scale nightside current system. We further argue that the conductance and convection electric field distributions provide support for a decoupling of the postmidnight and premidnight westward electrojet components.

Acknowledgments

For the ground magnetometer data, we gratefully acknowledge the following: Intermagnet; USGS, Jeffrey J. Love; Danish Meteorological Institute; CARISMA, Ian Mann; CANMOS; the S-RAMP database, K. Yumoto and K. Shiokawa; the SPIDR database; AARI, Oleg Troshichev; the MACCS program, M. Engebretson, Geomagnetism Unit of the Geological Survey of Canada; GIMA; MEASURE, UCLA IGPP, and Florida Institute of Technology; SAMBA, Eftyhia Zesta; 210 Chain, K. Yumoto; SAMNET, Farideh Honary; the institutes that maintain the IMAGE magnetometer array, Eija Tanskanen; PENGUIN; AUTUMN, Martin Connors; Greenland magnetometers operated by DTU Space; South Pole and McMurdo Magnetometer, Louis J. Lanzerotti and Alan T. Weatherwax; ICESAR; RAPIDMAG; PENGUIN; British Antarctic Survey; McMac, Peter Chi; BGS, Susan Macmillan; Pushkov Institute of Terrestrial Magnetism, Ionosphere and Radio Wave Propagation (IZMIRAN); SuperMAG, Jesper W. Gjerloev. For the Polar VIS Earth Camera images, we gratefully acknowledge the Polar VIS Earth Camera team that was led by Louis A. Frank at the University of Iowa.

Michael Liemohn thanks Gordon Rostoker and an anonymous reviewer for their assistance in evaluating this paper.

References

- Aruliah, A. L., I. C. F. Müller-Wodarg, and J. Schoendorf (1999), Consequences of geomagnetic history on the high-latitude thermosphere and ionosphere: Averages, *J. Geophys. Res.*, *104*(A12), 28,073–28,088, doi:10.1029/1999JA900334.
- Ahn, B. H., Y. Kamide, H. W. Kroehl, M. Candidi, and J. S. Murphree (1995), Substorm changes of the electrodynamic quantities in the polar ionosphere: CDAW 9, *J. Geophys. Res.*, *100*, 23,845–23,856, doi:10.1029/95JA02001.
- Akasofu, S.-I. (1964), The development of the auroral substorm, *Planet. Space Sci.*, *12*, 273–282.
- Allen, J. H., and H. W. Kroehl (1975), Spatial and temporal distributions of magnetic effects of auroral electrojets as derived from AE indices, *J. Geophys. Res.*, *80*, 3667–3677, doi:10.1029/JA080i025p03667.
- Clauer, C. R., and Y. Kamide (1985), DP1 and DP2 current systems for the March 22, 1979 substorms, *J. Geophys. Res.*, *90*, 1343–1354, doi:10.1029/JA090iA02p01343.
- Clauer, C. R., and R. L. McPherron (1974), Mapping the local time-universal time development of magnetospheric substorms using mid-latitude magnetic observations, *J. Geophys. Res.*, *79*, 2811–2820, doi:10.1029/JA079i019p02811.
- Donovan, E. (1993), Modelling the magnetic effects of field-aligned currents, *J. Geophys. Res.*, *98*, 13,529–13,543, doi:10.1029/93JA00603.
- Foster, J. C., J. P. St.-Maurice, and V. J. Aube (1983), Joule heating at high latitudes, *J. Geophys. Res.*, *88*, 4885–4897, doi:10.1029/JA088iA06p04885.
- Frank, L. A., J. D. Craven, K. L. Ackerson, M. R. English, R. H. Eather, and R. L. Carovillano (1981), Global auroral imaging instrumentation for the Dynamics Explorer mission, *Space Sci. Instrument*, *5*, 369–393.
- Frank, L. A., J. B. Sigwarth, J. D. Craven, J. P. Cravens, J. S. Dolan, M. R. Dvorsky, P. K. Hardebeck, J. D. Harvey, and D. Q. Muller (1995), The visible imaging system (VIS) for the Polar spacecraft, *Space Sci. Rev.*, *71*, 297–328.
- Fujii, R., R. A. Hoffman, P. C. Anderson, J. D. Craven, M. Sugiura, L. A. Frank, and N. C. Maynard (1994), Electrodynamic parameters in the nighttime sector during auroral substorms, *J. Geophys. Res.*, *99*, 6093–6112, doi:10.1029/93JA02210.
- Gjerloev, J. W. (2009), A global ground-based magnetometer initiative, *Eos Trans. AGU*, *90*(27), 230–231, doi:10.1029/2009EO270002.
- Gjerloev, J. W. (2012), The SuperMAG data processing technique, *J. Geophys. Res.*, *117*, A09213, doi:10.1029/2012JA017683.
- Gjerloev, J. W., and R. A. Hoffman (2000), Height-integrated conductivity in auroral substorms: 1. Data, *J. Geophys. Res.*, *105*, 215–226, doi:10.1029/1999JA900354.
- Gjerloev, J. W., and R. A. Hoffman (2001), The convection electric field in auroral substorms, *J. Geophys. Res.*, *106*, 12919.
- Gjerloev, J. W., and R. A. Hoffman (2002), Currents in auroral substorms, *J. Geophys. Res.*, *107*(A8), doi:10.1029/2001JA000194.
- Gjerloev, J. W., R. A. Hoffman, S. Ohtani, J. Weygand, and R. Barnes (2002), Response of the auroral electrojet indices to abrupt southward IMF turnings, *Ann. Geophys.*, *28*, 1167–1182.
- Gjerloev, J. W., R. A. Hoffman, J. Sigwarth, and L. A. Frank (2007), Statistical description of the bulge-type auroral substorm in the far ultraviolet, *J. Geophys. Res.*, *112*, A07213, doi:10.1029/2006JA012189.
- Gjerloev, J. W., R. A. Hoffman, J. B. Sigwarth, L. A. Frank, and J. B. H. Baker (2008), Typical auroral substorm: A bifurcated oval, *J. Geophys. Res.*, *113*, A03211, doi:10.1029/2007JA012431.
- Grocott, A., S. W. H. Cowley, J. B. Sigwarth, J. F. Watermann, and T. K. Yeoman (2002), Excitation of twin-vortex flow in the nightside high-latitude ionosphere during an isolated substorm, *Ann. Geophys.*, *20*, 1577–1601, doi:10.5194/angeo-20-1577-2002.
- Hoffman, R. A., J. W. Gjerloev, L. A. Frank, and J. W. Sigwarth (2010), Are there optical differences between storm-time substorms and isolated substorms?, *Ann. Geophys.*, *28*, 1183–1198.
- Kamide, Y., and W. Baumjohann (1985), *Magnetospheric-Ionospheric Coupling*, Springer-Verlag, New York.
- Kamide, Y., and S. Kokubun (1996), Two-component auroral electrojet: importance for substorm studies, *J. Geophys. Res.*, *101*, 13,027–13,046, doi:10.1029/96JA00142.
- Kamide, Y., A. D. Richmond, and S. Matsushita (1981), Estimation of ionospheric electric field, ionospheric currents, and field-aligned currents from ground based magnetic records, *J. Geophys. Res.*, *86*, 801–813, doi:10.1029/JA086iA02p00801.
- Kamide, Y., et al. (1982), Global distribution of ionospheric and field-aligned currents during substorms as determined from six IMS meridian chains of magnetometers: Initial results, *J. Geophys. Res.*, *87*, 8228–8240, doi:10.1029/JA087iA10p08228.

- Kamide, Y., W. Sun, and S. I. Akasofu (1996), The average ionospheric electrodynamics for the different substorm phases, *J. Geophys. Res.*, *101*, 99–109, doi:10.1029/95JA02990.
- Kisabeth, J. L., and G. Rostoker (1974), The expansive phase of magnetospheric substorms: 1. Development of the auroral electrojets and auroral arc configuration during a substorm, *J. Geophys. Res.*, *79*(7), 972–984, doi:10.1029/JA079i007p00972.
- Kisabeth, J. L., and G. Rostoker (1977), Modelling of three-dimensional current systems associated with magnetospheric substorms, *Geophys. J. R. Astron. Soc.*, *49*, 655–683.
- Lu, G. (2000), A synthetic view of the magnetospheric-ionospheric current system associated with substorms, in *Magnetospheric Current Systems*, edited by S.-I. Ohtani et al., AGU, Washington, D. C., doi:10.1029/GM118p0199.
- Lu, G., A. D. Richmond, Y. Kamide, D. Lummerzheim, M. Brittnacher, and G. Parks (1998), Global ionospheric convection during substorm expansion, in *Substorms-4*, edited by S. Kokubun and Y. Kamide, pp. 617–622, Kluwer Acad.
- Lyons, L. R., T. L. Killeen, and R. L. Walterscheid (1985), The neutral wind “flywheel” as a source of quiet-time, polar cap currents, *Geophys. Res. Lett.*, *12*, 101–104, doi:10.1029/GL012i002p00101.
- McPherron, R. L., C. T. Russell, and M. P. Aubry (1973), Satellite studies of magnetospheric substorms on August 15, 1968: 9. Phenomenological model of substorms, *J. Geophys. Res.*, *78*, 3131–3149, doi:10.1029/JA078i016p03131.
- Miyashita, Y., S. Machida, K. Liou, T. Mukai, Y. Saito, H. Hayakawa, C.-I. Meng, and G. K. Parks (2003), Evolution of the magnetotail associated with substorm auroral breakups, *J. Geophys. Res.*, *108*(A9), 1353, doi:10.1029/2003JA009939.
- Pellinen, R., T. Pulkkinen, and K. Kauristie (1994), Have we learned enough about auroral substorm morphology during the past 30 years?, Proceedings of the Second International Conference on Substorms, Fairbanks.
- Provan, G., M. Lester, S. B. Mende, and S. E. Milan (2004), Statistical study of high-latitude plasma flow during magnetospheric substorms, *Ann. Geophys.*, *22*, 3607–3624, doi:10.5194/angeo-22-3607-2004.
- Rees, M. H. (1963), Auroral ionization and excitation by incident energetic electrons, *Planet. Space Sci.*, *11*, 1209–1218.
- Richmond, A. D., et al. (1990), Global measures of ionospheric electrodynamic activity inferred from combined incoherent scatter radar and ground magnetometer observations, *J. Geophys. Res.*, *95*(A2), 1061–1071, doi:10.1029/JA095iA02p01061.
- Rostoker, G. (1996), Phenomenology and physics of magnetospheric substorms, *J. Geophys. Res.*, *101*, 12,955–12,973, doi:10.1029/96JA00127.
- Sigsbee, K., J. A. Slavin, R. P. Lepping, A. Szabo, M. Øieroset, M. L. Kaiser, M. J. Reiner, and H. J. Singer (2005), Statistical and superposed epoch study of dipolarization events using data from wind perigee passes, *Ann. Geophys.*, *23*(3), 831–851, doi:10.5194/angeo-23-831-2005.
- Spiro, R. W., P. H. Reiff and L. J. Maher, Jr. (1982), Precipitating electron energy flux and auroral conductivities: An empirical model, *J. Geophys. Res.*, *87*, 8215–8227, doi:10.1029/JA087iA10p08215.
- Torr, M. R., et al. (1995), A far ultraviolet imager for the international solar-terrestrial physics mission, *Space Sci. Rev.*, *71*, 329–383.
- Wallis, D. D., and E. E. Budzinski (1981), Empirical models of height integrated conductivities, *J. Geophys. Res.*, *86*, 125–137, doi:10.1029/JA086iA01p00125.
- Wiens, R. G., and G. Rostoker (1975), Characteristics of the development of the westward electrojet during the expansive phase of magnetospheric substorms, *J. Geophys. Res.*, *80*, 2109–2128, doi:10.1029/JA080i016p02109.
- Wing, S., J. W. Gjerloev, J. Johnson, and R. A. Hoffman (2007), Substorm plasma sheet ion pressure profiles, *Geophys. Res. Lett.*, *34*, L16110, doi:10.1029/2007GL030453.
- Winningham, J. D., and W. J. Heikkila (1974), Polar cap auroral electron fluxes observed with Isis 1, *J. Geophys. Res.*, *79*, 949–957, doi:10.1029/JA079i007p00949.